Gas transport parameters of differently compacted granulated bentonite mixtures (GBMs) under air-dried conditions

Nazir, Mazhar; Kawamoto, Ken; Sakaki, Toshihiro; Komatsu, Toshiko; Moldrup, Per

Published in:
Soils and Foundations

DOI (link to publication from Publisher):
10.1016/j.sandf.2022.101223

Publication date:
2022

Document Version
Publisher's PDF, also known as Version of record

HOSTED BY
ELSEVIER
Available online at www.sciencedirect.com
ScienceDirect
Soils and Foundations 62 (2022) 101223
www.elsevier.com/locate/sandf

Technical Paper

Gas transport parameters of differently compacted granulated bentonite mixtures (GBMs) under air-dried conditions ☆

Mazhar Nazir [a,*], Ken Kawamoto [a], Toshihiro Sakaki [b], Toshiko Komatsu [a], Per Moldrup [c]

[a] Graduate School of Science and Engineering, Saitama University, 255 Shimo-Okubo, Sakura-ku, Saitama 338-8570, Japan
[b] ESE Consulting LLC, Hyogo 662-0842, Japan
[c] Department of the Built Environment, Aalborg University, Thomas Manns Vej 23, DK-9220 Aalborg, Denmark

Received 31 January 2022; received in revised form 30 August 2022; accepted 5 September 2022
Available online 17 November 2022

Abstract

Granulated bentonite mixtures (GBMs) have been regarded as effective buffer materials in the deep geological disposal of radioactive waste due to their operational advantages, such as ease of transportation and in-situ placement/backfilling. Many studies have been done to characterize the hydraulic and thermal properties of GBMs as well as their swelling properties. Only limited studies, however, have investigated their gas transport properties, even though these properties affect their compactness during in-situ placement/backfilling and subsequent gas diffusion and advection in the buffer zone. The aim of this study is to understand the gas transport parameters, i.e., air permeability (k_a) and gas diffusivity (D_p/D_o), of tested samples compacted at different dry densities (DDs) under air-dried conditions, linking them with the measured density distribution characteristics determined by microfocus X-ray computed tomography (MFXCT) analysis. Two types of GBMs were used in this study: 1) FE-GBM (prepared from National Standard® bentonite, Wyoming, USA): this material was used in the Full-scale Emplacement (FE) experiment at the Mont Terri rock laboratory, Switzerland) and 2) OK-GBM (prepared from a bentonite, originating from Japan, with the trade name of OK bentonite, Kunimine Industries). The tested samples were firstly packed in a 100-cm^3 acrylic core with different DDs, ranging from loose to dense (1.09 to 1.75 g/cm^3), and scanned by MFXCT. The weighting factors, w_f (fine fraction; lower density) and w_c (coarse fraction; higher density) ($w_f + w_c = 1$), were determined after the peak separation of the measured CT brightness histograms from the reconstructed three-dimensional multiplanar reconstruction (MPR) images of the MFXCT analysis. The measured k_a and D_p/D_o were highly dependent on the DDs, the k_a (ε) values fitted well with a power law model, and the D_p/D_o (ε) was predicted accurately by several previously proposed models. For both FE-GBM and OK-

Abbreviations: DD, Dry density [g/cm^3]; EC, Electrical conductivity [mS/cm]; EDX, Energy-dispersive X-ray spectroscopy; FE, Full-scale Emplacement; FEBEX, Full-scale Engineered Barriers experiment; GBM, Granulated bentonite mixture; GSD, Grain size distribution; GDC, Generalized density-corrected D_p/D_o model (Chamindu Deepagoda et al., 2011); KC, Kozeny and Carman model (Kozeny, 1927, Carman, 1938 and 1956); LL, Liquid limit [%]; LOI, Loss on ignition [%]; MDD, Maximum dry density [g/cm^3]; MFXCT, Microfocus X-ray computed tomography; MPR, Multiplanar reconstruction image in MFXCT analysis; MQ, Millington and Quirk model (Millington and Quirk, 1961); NAGRA, National Cooperative for the Disposal of Radioactive Waste; PI, Plasticity index [–]; PL, Plastic limit [%]; RH, Relative humidity [%]; ROI, Region of interest in MFXCT analysis; SE, Standard error; SEM, Scanning electron microscopy; SSA, Specific surface area based on Brunauer–Emmett–Teller (BET) theory [m^2/g]; SR, Scanning resolution [μm/voxel]; C, Pore shape and tortuosity factor in KC model [–]; d_{50}, Mean diameter of grain [mm]; d_{eq}, Equivalent pore diameter [μm]; D_p/D_o, Gas diffusivity [–]; e, Void ratio [–]; G_S, Specific gravity [–]; k_a, Air permeability [μm^2]; P_{swell}, Swelling pressure [MPa]; S_v, Volumetric surface area measured by MFXCT analysis [1/mm]; T, Tortuosity [–]; V_P, Pore volume measured by Barrett-Joyner-Halenda (BJH) model [cm^3/g]; w_{AD}, Gravimetric water content at air-dried conditions [g/g in %]; w_c, Weighting factor of coarse fraction (estimated from CT brightness histogram in MFXCT analysis) [–]; w_f, Weighting factor of fine fraction (estimated from CT brightness histogram in MFXCT analysis) [–]; X_a, Pore connectivity-tortuosity factor in power law $k_a(\varepsilon)$ model; X_g, Pore connectivity-tortuosity factor in power law $D_p/D_o(\varepsilon)$ model; α, Constant in power law $k_a(\varepsilon)$ model; ε, Air-filled porosity [cm^3/cm^3]; θ, Volumetric water content [cm^3/cm^3]; Φ, Total porosity [cm^3/cm^3]

Peer review under responsibility of The Japanese Geotechnical Society.

* Corresponding author.
E-mail addresses: mazhar955@yahoo.com (M. Nazir), kawamoto@mail.saitama-u.ac.jp (K. Kawamoto), tsakaki.ese@gmail.com (T. Sakaki), komatsu@mail.saitama-u.ac.jp (T. Komatsu), pmol@build.aau.dk (P. Moldrup).

https://doi.org/10.1016/j.sandf.2022.101223

GBM, there were good linear relationships between the gas transport parameters and $w_c \times$ DD, implying that the weight of the coarse fraction controlled k_a and D_p/D_o. Moreover, the Kozeny-Carman model, incorporating the measured volumetric surfaces from the MFXCT analysis, was able to predict the k_a values well.

Keywords: Radioactive waste disposal; Buffer; Granulated bentonite mixtures (GBMs); Gas transport parameters; Microfocus X-ray computed tomography (MFXCT)

1. Introduction

The safe disposal of high-level radioactive waste (HLW) in deep geological environments is essential for the protection of the biosphere. In the concept of HLW repositories, metallic canisters containing HLW are embedded in the deep host rock surrounded by a buffer material (Dixon et al., 2011; Liu and Skoczylas, 2014; Villar et al., 2016). Bentonite has been regarded as a candidate buffer material due to its multifaceted characteristics, such as its high radionuclide retardation capacity, low permeability, high swelling capacity (Yong et al., 1986; Arthur et al., 2004; Wersin et al., 2007; Villar and Lloret, 2008), microporous structure (Wersin et al., 2007), plasticity (Arthur et al., 2004; Wersin et al., 2007), and thermal conductivity (Arthur et al., 2004). Compacted bentonite blocks have been tested as the main buffer in many design concepts. A number of technological issues were identified during the Full-scale Engineered Barriers experiment (FEBEX) project that might become critical during real emplacement operations in repositories, e.g., alignment of the steel liner with the drift axis and irregular rock surfaces in the drift (Mayor et al., 2005). The research has evolved and led to the adoption of granulated bentonite mixtures (GBMs) as effective buffer materials for some disposal systems in order to improve the barrier emplacement operations, e.g., easy transportation and in-situ placement in deep tunnels and holes, as well as to avoid the problems faced during the previously tested alternative systems (Alonso et al., 2010). In addition, GBMs comprise a practicable solution for sealing the gaps and cavities formed during excavations in rock (Mayor et al., 2005) as well as being a relatively low cost material (Masuda et al., 2007).

The emplacement dry density (DD) of GBMs as buffer/backfill materials is believed to be an important design parameter for ensuring the purported adequate long-term performance of the buffer (Müller et al., 2017; Nazir et al., 2021a). GBMs are to be emplaced at the required DDs with a relatively low initial water content for easier transportation. In the Full-scale Emplacement (FE) experiment implemented at the Mont Terri rock laboratory in Switzerland (Müller et al., 2017; Sakaki et al., 2022), an emplaced DD of 1.45 g/cm^3 was defined as the required minimum emplacement DD for the GBM used in this experiment, namely, a mixture prepared from highly compressed pellets (having an average pellet DD of 2.18 g/cm^3 and an average water content of 4.82 %) mixed with fine powders, considering the design requirements for the key parameters, such as hydraulic conductivity, swelling pressure, thermal conductivity, and microbiological activity (Garitte et al., 2015). Structural changes may occur as a result of compression during the emplacement of these GBMs and from the stress exerted by the surrounding rock due to the continuous creep deformation of the rock and the adjustment of stress in the excavation damaged zone (Liu et al., 2020). Although the compression-induced alterations in the pore structure involve macro-porosity (inter-pellet porosity), they are related to the water, gas, and thermal transport properties of the GBMs. Furthermore, water infiltration from the surrounding bedrock will cause the hydration of the GBMs, resulting in microstructural as well as macro-level changes, thus making the situation more complex. Therefore, a thorough understanding of the thermal, hydraulic, and mechanical (swelling, etc.) changes, as well as knowledge of the gas transport characteristics of GBMs, is essential for designing and implementing an efficient buffer for repositories (Cui et al., 2011; Nazir et al., 2021b).

Previous research on GBMs was mostly focused on the thermal (Masuda et al., 2007; Wieczorek et al., 2014; Sakaki, et al., 2019), hydraulic (Mayor et al., 2005; Masuda et al., 2007; Karnland et al., 2008; Yamada et al., 2014; Liu et al., 2020), and swelling properties (Sugita et al., 2003; Mayor et al., 2005; Imbert & Villar, 2006; Karnland et al., 2008; García-Siñeriz et al., 2015) of GBMs. As for the gas transport characteristics, most of the research has been conducted on highly compacted bentonites in the form of blocks, considering the bentonite blocks as the main buffer (Villar and Lloret, 2001; Villar et al., 2013; Carbonell et al., 2019; Harrington et al., 2019; Liu et al., 2020). However, the gas transport properties of GBMs have scarcely been investigated.

Different gaseous species (hydrogen, methane, and carbon dioxide) are produced in deep geological repositories by various mechanisms (Villar et al., 2013). The presence of oxygen (O_2) and its fate in a repository's near-field environment play a significant role in controlling the duration of the aerobic conditions. During the FE experiment at the Mont Terri rock laboratory, Switzerland, the O_2 concentration in the FE drift was monitored by O_2 sensors

installed at various locations in the drift to measure the oxygen concentration of the GBM's unsaturated pore spaces. The O_2 monitoring data (5 months of data recorded from November 2014 to April 2015) showed that the O_2 concentration in the GBM's pore spaces rapidly decreased during the backfilling process. Before the plug construction, H_2 gas was also detected in some of the collected gas samples, indicating localized anaerobic conditions. The results of the in-situ gas monitoring, laboratory testing, and modeling work showed that anaerobic conditions in the repository may be reached within a very short time span, ranging from a few weeks up to a few months, after the closure of the emplacement drift. The relative humidity (RH) monitoring data from the same FE experiment showed that the RH in the GBM ranged from 40 to 50 % in the same time span as the O_2 monitoring (Giroud et al., 2018). As such repositories will be constructed in deep rock formations with low hydraulic conductivity (Müller et al., 2017), the GBM may be subjected to unsaturated conditions for a longer time (due to a limited inflow from the surrounding rock), and the gas generation in the repository and its transport through the emplaced GBM may occur prior to the increase in RH levels in the GBM. Therefore, understanding the gas transport characteristics of the GBM at the initial emplaced state is also an essential parameter for the design of buffers.

The transport of gases through porous media is governed by advection and diffusion; the former occurs under an air pressure gradient and the latter under a gas concentration gradient (Hamamoto et al., 2009; Carbonell et al., 2019). Air permeability, [k_a (μm^2)], is the controlling transport parameter for the advective gas flow, whereas gas diffusivity, D_p/D_o (D_p is the soil gas diffusion coefficient [m^2/s] and D_o represents the gas diffusion coefficient in free air [m^2/s]), is the governing transport parameter for the diffusive transport. At the outset of gas generation in a repository, the gas moves predominantly due to diffusion brought about by a low gas generation rate (Liu et al., 2015). If the gas generation rate is higher than the gas diffusion rate, gas continues to accumulate until advective flow occurs (Harrington et al., 2019) due to the pressure gradients resulting from the gas generation, temperature changes, and changes in the pore network system caused by the varying stress state and humidity conditions in the repository (Villar and Lloret, 2001). The gas migration through porous soils is affected by various soil physical parameters, such as particle size distribution, DD, moisture content (or degree of saturation), and pore structure parameters, including air-filled porosity and total porosity as well as pore connectivity-tortuosity (Hamamoto et al., 2009). Liu et al. (2016) studied the effect of the water content on the gas permeability of GBM core specimens extracted during the dismantling of the Engineered Barrier Emplacement experiment (EB) conducted at Mont Terri rock laboratory, Switzerland. Their results indicated that gas permeability decreased with an increase in water content. At the same water content, despite the very discrete gas permeability values that were measured, it was noted that the effect of the DD (which governs the air-filled porosity available for the gas flow) on the gas permeability of the GBM should also be considered for a better interpretation of the results and to arrive at a conclusion. Villar et al. (2013) also observed from gas permeability experiments, conducted within the framework of the compacted bentonite blocks concept, that the DD greatly affected the gas permeability of compacted bentonite block samples tested at a similar water content, namely, the gas permeability decreased by about three orders of magnitude with an increasing DD from 1.5 to 1.8 g/cm^3.

In this study, the gas transport parameters, air permeability, k_a, and gas diffusivity (D_p/D_o) of GBM samples, prepared at different DDs, were investigated. The MFXCT system was used to understand the compaction (density distribution) characteristics of the same GBM samples. The characteristic parameters from the MFXCT results were correlated with the gas transport parameters, k_a and D_p/D_o. In addition, the volumetric surface areas (S_v) of the same GBM samples were calculated by MFXCT analyses that were used to predict k_a.

2. Materials and methodologies

2.1. Material characterization and sample preparation

Two types of GBMs, FE-GBM and OK-GBM, were used in this study. The FE-GBM is a mixture prepared from parent bentonite with the commercial name of National Standard®, Wyoming, USA (Garitte et al., 2015). This mixture was used in the FE experiment at the Mont Terri rock laboratory, Switzerland (Müller et al., 2017). The OK-GBM is a mixture prepared from a granulated bentonite from Japan (trade name of OK bentonite, Kunimine Industries, Japan). This material is from a similar ore of origin to Kunigel V1 (Nakashima et al., 2014). The detailed procedure for the production process of the GBM/pellets is given in the LUCOEX project report (Garitte et al., 2015) and previous research studies (Nakashima et al., 2014). Fig. 1 shows photos of the two materials; the apparent color of the FE-GBM is grey, while that of the OK-GBM is whitish-grey. The main objective of using GBMs is to increase the DD of raw bentonite to the required emplaced DD according to the repository design requirements (Garitte et al., 2015). The FE-GBM was obtained from NAGRA. The mixture was sieved through meshes of various sizes; the measured grain size distribution (GSD) of the FE-GBM is shown in Fig. 2. The GSD curve essentially follows Fuller's grading (Fuller and Thompson, 1907); the upper and lower limits of the target Fuller's curve for this material defined by Garitte et al. (2015) are also plotted in Fig. 2. The Fuller function maximizes the density by relating the GSD to the largest grain size. It is described by [$p = (d/D)^n \times 100$], where p is the percentage of weight passing through a sieve of size

Fig. 1. Photos of materials tested in this study: (a) FE-GBM and (b) OK-GBM.

d, D is the largest grain size, and n is a shape parameter. Previous studies on the GSD of GBMs suggested that the optimum results (high density packing, lowest porosities, and least segregation) can be achieved following a GSD that matches Fuller's distribution (de Bock et al., 2009; Garitte et al., 2015; NAGRA, 2019). A granular material of OK-bentonite ore was obtained from the manufacturer with pellets of sizes $\leq$ 30 mm. The pellets were crushed and separated into different sizes by sieving, e.g., 9.5 to 4.75 mm, 4.75 to 2 mm, 2 to 0.85 mm, 0.85 to 0.425 mm, 0.425 to 0.25 mm, 0.25 to 0.106 mm, and $<$ 0.106 mm, and subsequently mixed in weighed proportions following the percentage passing of the FE-GBM from the GSD for adaptation to the same distribution. Both materials, FE-GBM and OK-GBM, were stored in a climate-controlled room under air-dried conditions (RH = 60 % and temperature = 20 °C) to avoid any adverse influences from changes in the ambient temperature or RH. Gas transport experiments and saturated swelling pressure tests were also conducted on these materials in the same air-dried environment (RH = 60 % and temperature = 20 °C).

The basic physical and chemical properties of the two materials tested in this study, along with the values reported in the literature, are given in Table 1. The reported index properties of other bentonite mixtures investigated worldwide, such as Kunigel V1 pellets, MX-80 GBM, Serrata GBM, and FOCA pellets/powder, are also summarized in Table 1 for comparison. The gravimetric water content (w_{AD}) of the tested FE-GBM sample under air-dried conditions (RH = 60 % and temperature = 20 °C) was 5.84 %, while the w_{AD} of the OK-GBM sample ranged from 6.38 to 8.66 %. A comparison of the DDs of the pellets shows that the pellet DD of most GBMs is around 2.0 g/cm^3, with a higher value of 2.18 g/cm^3 for the FE-GBM pellets of $<$ 10 mm (Garitte et al., 2015) and lower values of 1.81 to 1.84 g/cm^3 for the OK-GBM pellets of 20 to 30 mm (Nakashima et al., 2014). The plasticity index of the national standard bentonite (FE-GBM) is higher than that of all other bentonites. The maximum dry density (MDD) of the air-dried FE-GBM and OK-GBM samples was determined by modified Proctor compaction energy (E_c = 2700KJ/m^3). The specific surface area (SSA) was measured by the Brunauer–Emmett–Teller (BET) method (Brunauer et al., 1938). The SSA of the FE-GBM was almost twice that of

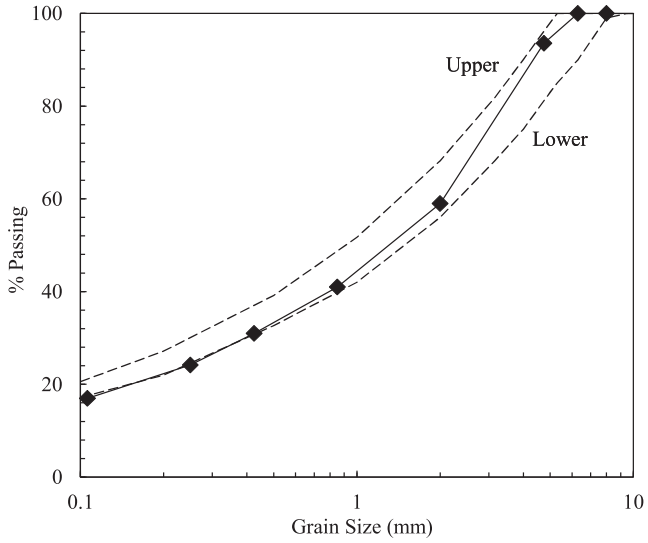

Fig. 2. The measured grain size distribution (GSD) for FE-GBM, as well as upper and lower Fuller limit curves (Garitte et al., 2015) for FE-GBM. The GSD for OK-GBM was created by sieving and mixing to become fully similar to the shown GSD for FE-GBM, see explanation in the main text.

the OK-GBM. In comparison, the Serrata GBM has the larger BET SSA, while the OK-GBM has the smallest BET SSA, amongst the various materials. The pore volume (V_p) was measured by the Barrett-Joyner-Halenda (BJH) model (Barrett et al., 1951) under adsorption. The pH and EC were measured at a liquid (milli-Q water)/solid ratio of 10.

Table 2 shows the chemical and mineral compositions of the materials used in this study and the values of other mixtures/bentonites in the literature. The bulk chemical compositions of the FE-GBM and OK-GBM were analyzed by energy-dispersive X-ray spectroscopy (EDX). The materials have identical chemical compositions; however, their proportions vary. Interestingly, the OK and Kunigel V1 bentonites contain higher SiO_2 and lower Al_2O_3 contents amongst the tabulated materials. The proportions of various elements (Si, Al, Ca, Fe, Na, Mg, and O) were measured by an energy-dispersive X-ray spectroscopy (EDS) analyzer. For reference, the SEM images, results of element mapping, and observed spectrums by an EDS analyzer for the FE-GBM and OK-GBM are shown in Figs. A1 and A2 **(Appendix A)**, respectively. The average elemental percentage values, measured from 30 spectra, are presented in Table 2. A comparison of the quantitative mineralogical compositions in the literature shows that, except for the OK and Kunigel V1 bentonites (Japanese origin), all other bentonites are rich in montmorillonite (≥80 %), which is a key component in swelling. Conversely, the OK bentonite and Kunigel V1 have higher fractions of quartz contents compared to the other bentonites.

The swelling characteristics of FE-GBM and OK-GBM under fully saturated conditions were measured in a rigid constant volume cell (with an internal ring diameter of 6 cm and a height of 1 cm). The GBM samples were packed in the ring at the target DDs (that of the FE-GBM ranging from 1.25 to 1.65 g/cm^3 and that of the OK-GBM ranging from 1.09 to 1.65 g/cm^3). After packing the samples and finishing the test setup, the samples were saturated with tap water. The axial swelling force was monitored and recorded with the help of a force transducer and data logger. The swelling test was terminated when the axial force became almost constant. The swelling pressure (P_{swell}) was calculated by dividing the axial force by the cross-sectional area of the ring. The experiments validated the DD-dependent swelling characteristics of both materials **(**Fig. 3**)**. The FE-GBM developed about 5-fold higher swelling pressure (P_{swell}) than the OK-GBM, with a sharply increasing trend, due to its abundant montmorillonite. Both the FE-GBM and OK-GBM data indicated a linear increase in P_{swell} with DD in the investigated DD ranges as represented by the best fit linear equations in Fig. 3. The measured P_{swell} values of the FE-GBM are seen to lie in the range of the P_{swell} of MX-80 and Serrata-GBM, while the P_{swell} values of the OK-GBM are seen to lie in the range of the P_{swell} of Kunigel V1 and FoCa.

For the MFXCT measurements and gas transport experiments (k_a and D_p/D_o), the air-dried materials (at RH = 60 %, temperature = 20 °C) were hand-packed at various DDs, ranging from loose to dense, into the acrylic cores of 100 cm^3 (diameter of 5.61 cm and height of 4.06 cm). The FE-GBM samples were prepared at DDs ranging from 1.25 to 1.75 g/cm^3, while the OK-GBM samples were prepared at DDs ranging from 1.09 to 1.75 g/cm^3. The materials were packed, without force, at loose to medium compaction. However, the densely packed samples were prepared by tapping the GBM with a small wooden rod.

Considering soil as a three-phase system (solid, water and air), the total porosity (Φ) in a soil system can be defined as.

$$\Phi = \varepsilon + \theta \tag{1}$$

where Φ is the total porosity (cm^3/cm^3), ε is the air-filled porosity (cm^3/cm^3), and θ is the volumetric water content (cm^3/cm^3). The gas transport through a soil system is strongly affected by the phase parameters given in Equation (1). Fig. 4 shows the variations in Φ, ε and θ based on the DD ranges investigated in this study. Phase relation equations were used to calculate these parameters: $\Phi = 1 - (DD/Gs)$, $\theta = DD \times w_{AD}$, and thus, $\varepsilon = \Phi - \theta$. It can be observed from this figure that ε progressively decreased with an increasing DD for both materials. However, θ varied slightly with the DD, and the values were approximately 0.1 cm^3/cm^3 for both materials. The degrees of saturation for the FE-GBM and OK-GBM samples varied from 14 to 29 % and 16 to 34 %, respectively.

2.2. Methodologies

2.2.1. MFXCT measurements and analyses

For the visualization of the density distribution characteristics by MFXCT, the packed GBM samples were firstly scanned using a MFXCT system (InspeXio SMX-90CT, Shimadzu Co. ltd., Japan). The adopted scanning and energy parameters were: scanning resolution (SR) = 20 μm/voxel conditions, number of slices = 540, image size of each slice = 1024 × 1024 pixels, number of views = 1800, average number for scanning = 4, scaling factor = 150, with the energy level of the machine at 90 kV and 110 μA. Multiplanar reconstruction (MPR) images were created from the reconstruction of the scanned sample slices. A 3D block of a region of interest (ROI) with 500 × 500 × 500 voxels (10 × 10 × 10 mm size) was selected from the MPR images of each sample and processed by the 3D image analysis software ExFact VR 2.1 (Nihon Visual Science Inc., Japan) to create a CT brightness histogram. The CT brightness histograms were then analyzed for peak separation in the peak fitting software, PeakFit v4.12 (Systat Software, Inc., USA) (Fig. 5**)**. For the measurement of S_v, the scanned MPR data of the GBM samples were analyzed using an EXFact analysis for porous particles (Nihon Visual Science Inc., Japan), at the ROI of 300 × 300 × 300. The EXFact analysis software was employed to calculate the S_v from the volumes

Table 1
Basic physical and chemical properties of materials tested in this study and values reported in the literature.

Parameter	Unit	FE-GBM (This study; Garitte et al., 2015)	OK-GBM (This study; Nakashima et al., 2014)	Kunigel V1 (JNC, 2000; Sugita et al., 2003; Komine, 2004)	MX-80 GBM (Villar, 2013; Plötze and Weber, 2007; Tang and Cui, 2005; Garitte et al., 2015)	Serrata GBM (Villar and Gómez-Espina, 2009; Hoffman et al., 2007)	FoCa (Volckaert et al., 2000)
G_s	–	2.72	2.62	2.7–2.79	2.75	2.7 ± 0.04	2.67
DD of pellets	g/cm^3	2.18	1.81–1.84	1.905	2.0	1.95	2.05
w_{AD}	%	5.84	6.38–8.66	–	–	–	–
LL (<0.425 mm)	%	628	387	473.9	519	102 ± 4	112
PL (<0.425 mm)	%	56	30	26.6	35	53 ± 3	50
PI	–	573	357	447.3	484	49 ± 1	62
MDD	g/cm^3	1.84	1.65	–	–	–	–
SSA (0.106–2 mm)	m^2/g	27.63	14.61	–	16–22	32 ± 3	–
SSA (<0.106 mm)		26.81	12.11	–			–
V_P (0.106–2 mm)	cm^3/g	6.36×10^{-2}	3.07×10^{-2}	–	–	–	–
V_P (<0. 106 mm)		6.83×10^{-2}	3.38×10^{-2}	–	–	–	–
LOI	%	5.94	4.37	–	–	–	–
pH	–	10.2	10.1	–	9.5	–	–
EC	mS/cm	0.896	0.903	–	–	–	–

Table 2
Chemical and mineral compositions of materials tested in this study and values reported in the literature.

Parameter	FE-GBM (This study; Garitte et al., 2015)	OK-GBM [a] (This study)	Kunigel V1 (Suzuki et al., 1992; JNC, 2000)	MX-80 GBM (Garitte et al., 2015)	Serrata GBM (ENRESA, 2000; Villar, 2002)	FoCa (Coulon, 1987; Villar, 2004; Guillot et al., 2002)
Bulk chemical composition (<2mm): Unit in %						
SiO_2	63.9	73.7	69.9	60.8	58.7 ± 1.9	56.7
Al_2O_3	20.6	14.4	14.4	19.0	18.0 ± 0.7	26.6
CaO	1.3	2.3	1.87	1.2	1.8 ± 0.1	1.08
Fe_2O_3	2.1	2.1	1.91	3.6	3.1 ± 0.1	7.94
Na_2O	1.5	1.9	2.7	2.0	1.3 ± 0.1	2.45
MgO	4.9	1.5	1.86	2.3	4.2 ± 0.1	2.29
Others	5.7	4.1	7.36	11.1	12.9	2.94
Element composition (<0.106 mm): Unit in weight %						
Si	32.9	38.8	–	–	–	–
Al	14.0	13.4	–	–	–	–
Ca	1.6	1.3	–	–	–	–
Fe	4.6	2.0	–	–	–	–
Na	0.9	1.3	–	–	–	–
Mg	1.9	1.8	–	–	–	–
O	43.0	41.5	–	–	–	–
Mineral composition: Unit in %						
Montmorillonite (Smectite)	80	46–49	46–49	86	92 ± 3	85–90[b]
Quartz	7.0	29–38	29–38	4.4	2 ± 1	6
Illite (Muscovite)	3.2(0.4)	–	–	(1.7)	–	–
Feldspar	4.0	2.7–5.5	2.7–5.5	5.3	–	–
Gypsum	–	–	–	0.6	0.14 ± 0.01	0.4
Plagioclase	3.0	–	–	–	2 ± 1	–
Pyrite	0.3	0.5–0.7	0.5–0.7		0.02 ± 0.01	–
Calcite	1.2	2.1–2.6	2.1–2.6	0.5	–	1.4
Siderite	0.3	–	–	–	–	–
Cristobalite	1.1	–	–	2.0	2 ± 1	–
Dolomite	–	2.0–2.8	2.0–2.8	–	0.60 ± 0.13	–
Zeolites	–	3.0–3.5	3.0–3.5	–	–	–
Kaolinite	–	–	–	–	–	4

[a] Data from Kunigel-V1 (Nakashima et al., 2014; same mineral ore as OK-GBM); [b] Interstratified beidellite and kaolinite (50/50% each).

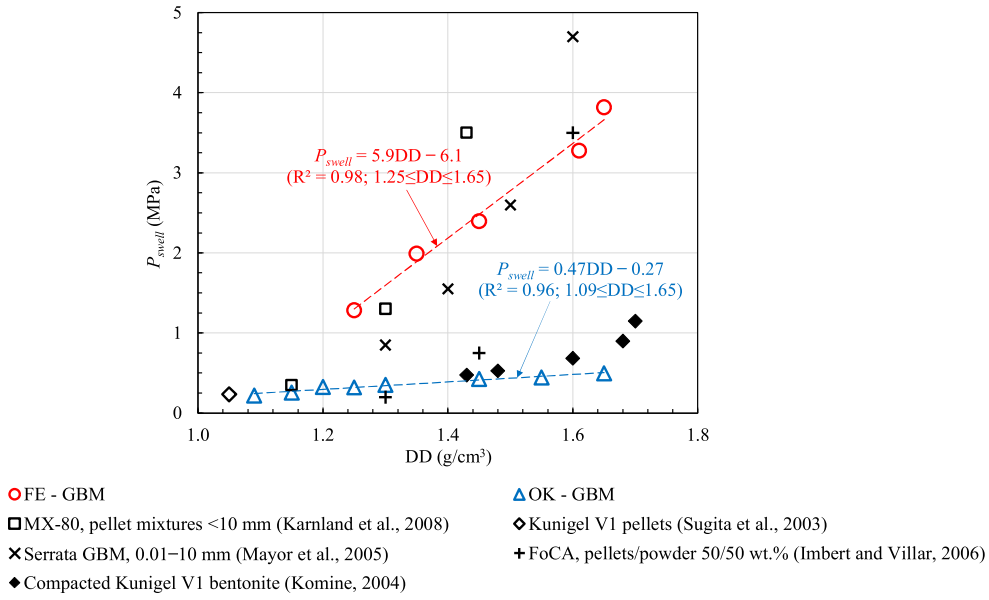

Fig. 3. Measured P_{swell} as a function of DD.

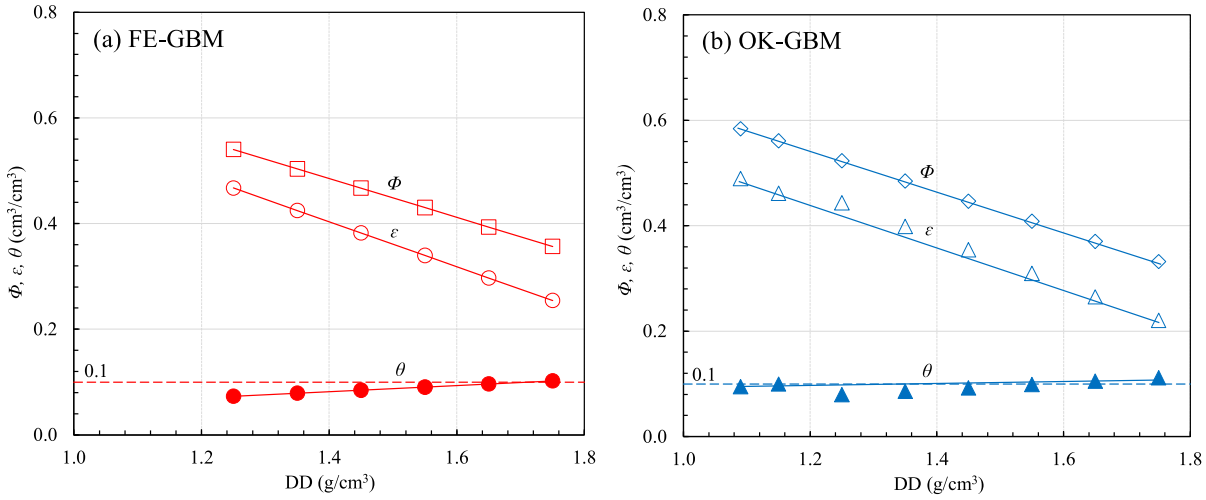

Fig. 4. Phase distribution of tested samples with different DD: (a) FE-GBM and (b) OK-GBM. The θ was calculated by using DD and a fixed measured initial water content (w_{AD}) of tested sample.

and surface areas of the grains from the segmented volumes. The detailed segmentation and calculation procedures are explained in Hamamoto et al. (2016).

2.2.2. Measurement of gas transport parameters

After the MFXCT scanning, the same samples were then used to measure the k_a and D_p under air-dried conditions (RH = 60 % and temperature = 20 °C) in a climate-controlled room. The k_a was measured using an air permeameter developed by Iversen et al. (2001). The equipment consists of four major components: 1) a compressed air cylinder supported by a pressure regulator to control the flow, 2) a set of flow meters (covering different flow ranges) to measure the flow rate, 3) a manometer to measure the air pressure difference, and 4) a sample holder. Air flow (generated by an air cylinder), at a constant small pressure difference, was applied to the sample, and the resulting air flow rate was measured using the flow meter. Darcy's equation was used to calculate the k_a from the measured flow rate and air pressure difference.

The gas diffusion through the packed GBM samples was measured by the diffusion chamber method (Currie, 1960; Rolston and Moldrup, 2002). The diffusion chamber consists of a diffusion vessel (at the bottom) and a sample holder (at the top) supported by a sliding plate between the sample holder and the diffusion chamber. The diffusion vessel contains inlet and outlet ports, for the flushing of gas, as well as an oxygen (O_2) sensor connected to a data

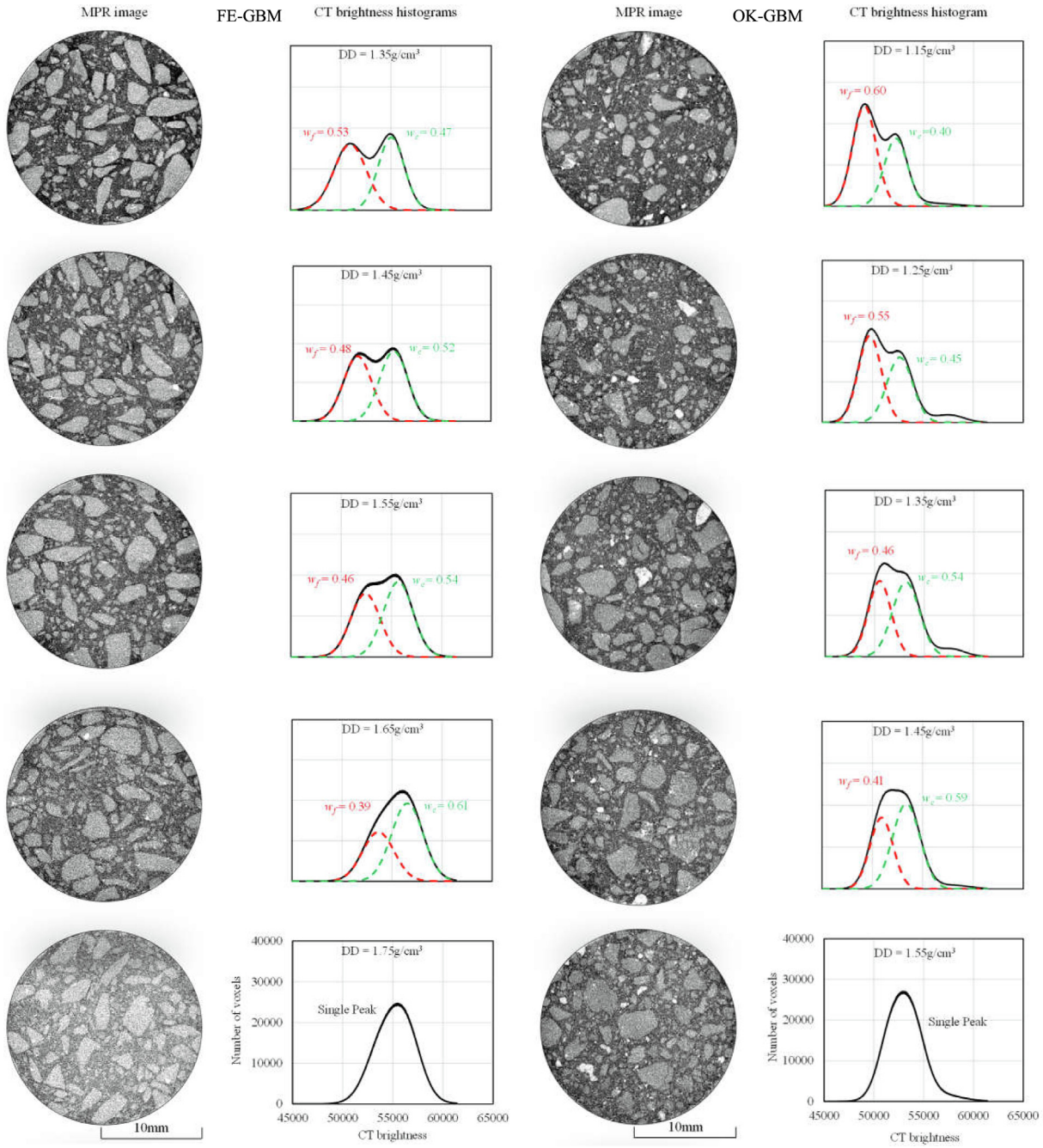

Fig. 5. MFXCT analyses results; MPR Images and CT brightness histograms of tested samples with different DD (SR = 20 μm/voxel, ROI = 500 × 500 × 500 voxels). Weighting factors, w_f and w_c, are given in the histograms.

logger to measure the change in the O_2 concentration. During the experiment, one end of the sample was connected to the diffusion vessel and the other end was kept exposed to air. Firstly, nitrogen (N_2) gas was supplied to the diffusion chamber until the O_2 (oxygen in the air at the controlled RH of 60 % and temperature of 20 °C) in the vessel was replaced by N_2. Subsequently, the N_2 was allowed to pass through the GBM sample by the binary diffusion process; the N_2 from the vessel diffused through the sample in the air and the air in the room diffused through the sample in the vessel. The increase in the O_2 concentration in the chamber during the diffusion process was measured every 30 s by the O_2 sensor connected to the data logger. The data recording was continued until all the N_2 in the chamber was replaced by O_2. The gas diffusion coefficient, D_p, was calculated according to Osozawa (1987) using the monitored O_2 concentration data. In order to calculate the gas diffusivity, D_p/D_o, the gas diffusion coefficient of O_2 in the free air (D_o) at 20 °C was taken as 0.20 cm^2/s (Currie, 1960; Glinski and Stepniewski,1985).

3. Predictive models for gas transport parameters

3.1. Predictive air permeability (k_a) models

k_a is generally represented in the form of (i) the power law function of ε (Moldrup et al., 2001, 2003; Kawamoto et al., 2006) or (ii) the classical Kozeny-Carman (KC) model void ratio function, $e^3/(1+e)$ (Kozeny, 1927; Carman, 1938, 1956). The power law and KC models, in their general forms, can be written as Eqs. (2) and (3), respectively:

$$k_a = \alpha\varepsilon^{X_a} \tag{2}$$

where α is a constant related to pore connectivity and X_a is a pore connectivity-tortuosity factor.

$$k_a = \frac{1}{CS_V{}^2}\frac{e^3}{1+e} \tag{3}$$

where C is the pore shape and tortuosity factor, S_v is the volumetric surface area (1/mm), and e is the void ratio. These two predictive models (power law and KC models) were used to explain the k_a characteristics of GBMs.

3.2. Predictive gas diffusivity (D_p/D_o) models

Like k_a, the D_p/D_o of soils is also typically described by the power function (X_g) of ε as suggested by Buckingham (1904), where X_g is a dimensionless exponent representing pore connectivity–tortuosity. Buckingham (1904) proposed a constant value of $X_g = 2$. Subsequently, many studies have incorporated the effects of soil type and density into their gas diffusivity models, such as the Millington and Quirk (MQ: 1960, 1961) model, and the more recently developed generalized density-corrected (GDC) model (Chamindu Deepagoda et al., 2011) that also provided satisfactory results when tested against the different soil aggregate size fractions. A detailed literature review of the predictive models was conducted. The following three well-known models, Buckingham (1904) – (4), MQ (1961) – (5), and GDC (2011) – (6), were used to interpret the D_p/D_o of GBMs.

$$D_p/D_o = \varepsilon^2 \tag{4}$$

$$\frac{D_p}{D_o} = \frac{\varepsilon^{10/3}}{\Phi^2}. \tag{5}$$

$$D_p/D_o = 0.5\Phi(\varepsilon/\Phi)^3 \tag{6}$$

3.3. Statistical analysis

The performance of the predictive D_p/D_o models was evaluated by two statistical parameters, the root-mean square error (RMSE) and the bias. The RMSE (Eq. 7) describes the overall model fitted to the measured data, and the bias (Eq. 8) indicates the model overestimation or underestimation as compared to the measured data.

$$\mathrm{RMSE} = \sqrt{\frac{1}{n}\sum_{i=1}^{n} d_i^2} \tag{7}$$

$$\mathrm{bias} = \frac{1}{n}\sum_{i=1}^{n} d_i \tag{8}$$

where d_i is the difference between the measured and the estimated values, and n is the number of measurements in the data set.

4. Results and discussion

4.1. MFXCT analysis and histograms of CT brightness

The results of the MFXCT measurements and analyses; MPR images and CT brightness histograms as well as the peak separation results (curves) are shown in Fig. 5. Under loosely packed conditions (i.e., low DD), a bimodal distribution (two peaks as shown in the histograms) was observed in both materials. The peak at the low CT brightness represents fines and pores, whereas the other peak at the high CT brightness represents the dense coarser pellets. The dark regions in the MPR images are the zones of low CT brightness (or low density), consisting of fines and pores, while the bright coarser regions are the zones of high CT brightness (or high density). The adopted MFXCT resolution (due to the limitation of the MFXCT equipment) was insufficient to distinguish the fine powders from the pore spaces around them. With increasing compaction (DD), the dark regions gradually diminished, and the dual peaks progressively merged into a single peak with a unimodal response, as can be seen in the histograms at DDs of 1.75 g/cm^3 (FE-GBM) and 1.55 g/cm^3 (OK-GBM). The MPR images corresponding to these unimodal histograms also show the existence of minimal dark regions at higher DDs, implying that the fines are tightly packed between the coarse particles, and the sample is considered to be a compacted mixture at this stage. In the OK-GBM, the unimodal histogram first appeared at a DD of 1.55 g/cm^3; the samples at DDs of 1.65 and 1.75 g/cm^3 also yielded unimodal histograms (the results are not shown here). This implies that compacted conditions in the OK-GBM were reached at the DD of 1.55 g/cm^3 and that further compaction could cause the crushing/breakage of the pellets. From the CT brightness values, it is seen that the average CT brightness increased with the increase in sample DD (Otani et al., 2000; Nazir et al., 2021b), and that the center of the peaks moved to the right until they merged to a single peak center. The MPR images also showed a change in color at the various DDs; a relatively black or dark grey color indicates low density (low CT brightness), while a white or light grey color indicates high density (high CT brightness). These findings are in line with the results of Otani et al. (2000). Furthermore, the overall CT brightness values of the FE-GBM were slightly higher than those of the OK-GBM. This may be attributed to the

higher pellet DD or other material properties of the FE-GBM.

To study the effects of the fine and coarse fractions on the gas transport parameters, a peak separation procedure for the dual peak histograms was adopted. From the peak separation results, weighting factors w_f and w_c were assigned to the peaks to develop a possible correlation between the MFXCT results and the measured gas transport parameters, where w_f represents a weighting factor for fine fractions having low CT brightness values and w_c represents a weighting factor for coarse fractions having high CT brightness values. The values for w_f and w_c are shown in Fig. 5. With the increasing DD, w_f and w_c decreased and increased, respectively. Numerically, the summation of these two factors is equal to unity and can be written as follows:

$$w_f + w_c = 1$$

4.2. Gas transport parameters in differently compacted GBMs

4.2.1. Interpretation of measured k_a and D_p/D_o

The measured k_a and D_p/D_o, under air-dried conditions, are presented as functions of ε in Fig. 6. Both k_a and D_p/D_o decreased non-linearly with the reduction in ε because compaction caused a decrease in ε. Higher k_a and D_p/D_o values are observed for the OK-GBM as compared to the FE-GBM. The gas transport processes through these materials can be explained by the pore structural parameters, such as the equivalent pore diameter (d_{eq}) (Ball, 1981), pore tortuosity (T) (Moldrup et al., 2001), and pore connectivity-tortuosity (X_g), which are given by the following equations:

$$d_{eq} = 2\sqrt{\frac{8\,k_a}{D_p/D_o}} \tag{9}$$

$$T = \sqrt{\frac{\varepsilon}{D_p/D_o}} \tag{10}$$

$$X_g = \frac{\log D_p/D_o}{\log \varepsilon} \tag{11}$$

Fig. 7 shows the values of these pore structure parameters. Initially, at a low dry density (higher $\varepsilon = 0.47$), the d_{eq} was almost similar (about 36 μm) in the two materials, as shown in Fig. 7(a). However, with increasing compaction, the d_{eq} in the FE-GBM drastically decreased to a minimum value of about 5 μm in the densely packed condition. The d_{eq} in the FE-GBM was about half that of the OK-GBM at the minimum ε value (≈ 0.25). As shown in Fig. 7(b), the T of the FE-GBM is higher than that of the OK-GBM in all the tested samples. The T values of the FE-GBM samples ranged from 1.6 to 2.3, while those of the OK-GBM samples ranged from 1.2 to 1.9. In the loosely packed condition, the T value of the OK-GBM was very low ($\approx$ 1.2 at ε = 0.49). However, with increasing compaction, the T value sharply increased to 1.6 at a corresponding ε of 0.4. Afterwards, a gentle increase in T was noted with further compaction (from ε = 0.4 to ε = 0.22). This trend can possibly be explained by the decrease in size of the flow channels (d_{eq}) with increasing compaction (Fig. 7a) in the OK-GBM. At a higher ε value (=0.49), larger pore channels exist which drastically decrease with compaction up to $\varepsilon = 0.4$, resulting in a sharp increase in T. The calculated T values in the FE-GBM are greater than the reported T values of other geomaterials (sands, loam, and silty clay loam soils), in the literature, at similar ε corresponding to the densely packed condition. In the loosely packed condition, however, the FE-GBM T values were approximately the same as those of silty clay loam. The X_g of the FE-GBM was also higher than that of the OK-GBM at identical ε values (Fig. 7c). Interestingly, the calculated minimum X_g values of the FE-GBM were even higher than those of Buckingham (1904,

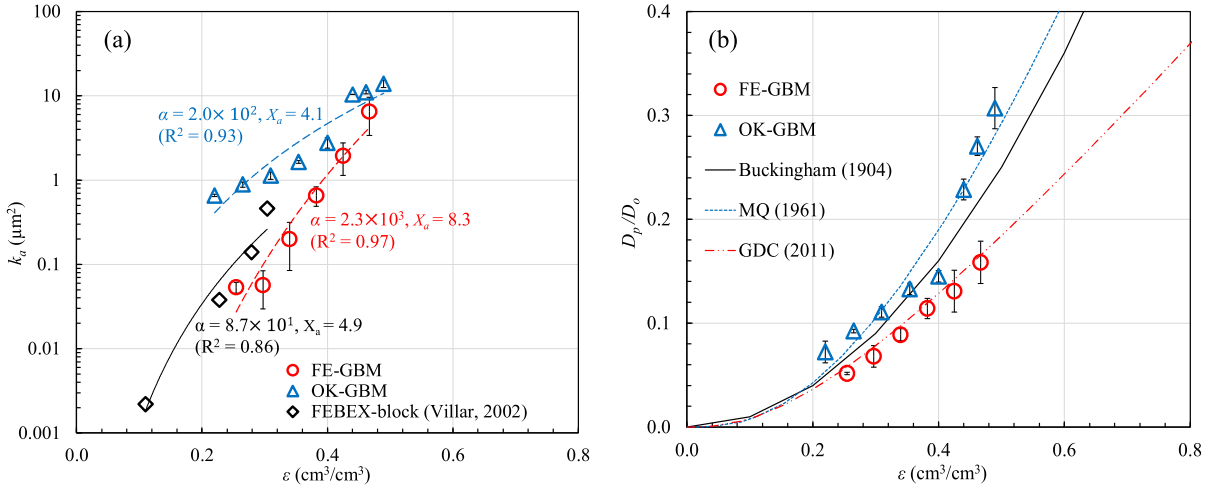

Fig. 6. (a) Measured k_a as a function of ε. Fitted values of $k_a = \alpha\varepsilon^{Xa}$ (Eq. 2) and literature data are given. (b) D_p/D_o as a function of ε. Predictive D_p/D_o models against measured data are given.

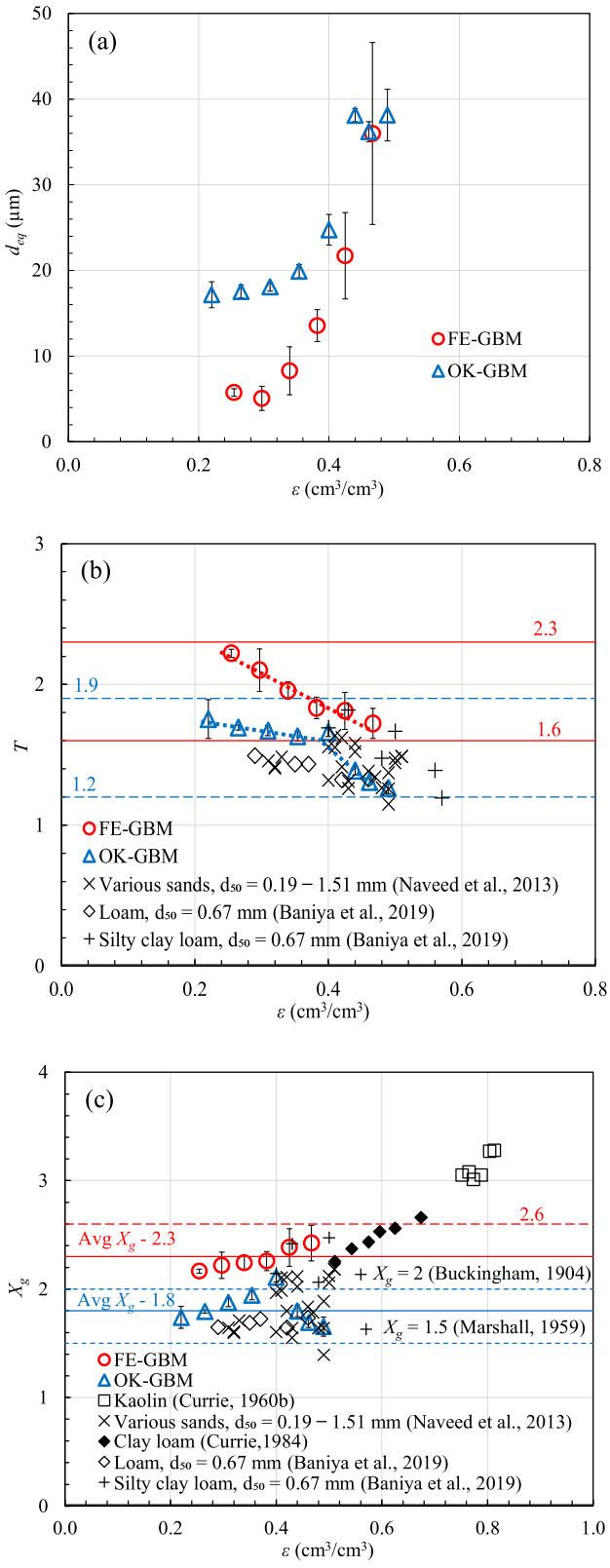

Fig. 7. The calculated (a) Equivalent pore diameter (d_{eq}), (b) tortuosity (T), and (c) pore connectivity-tortuosity factor (X_g) as a function of ε. The reported T and X_g values for various soils in the literature are also plotted.

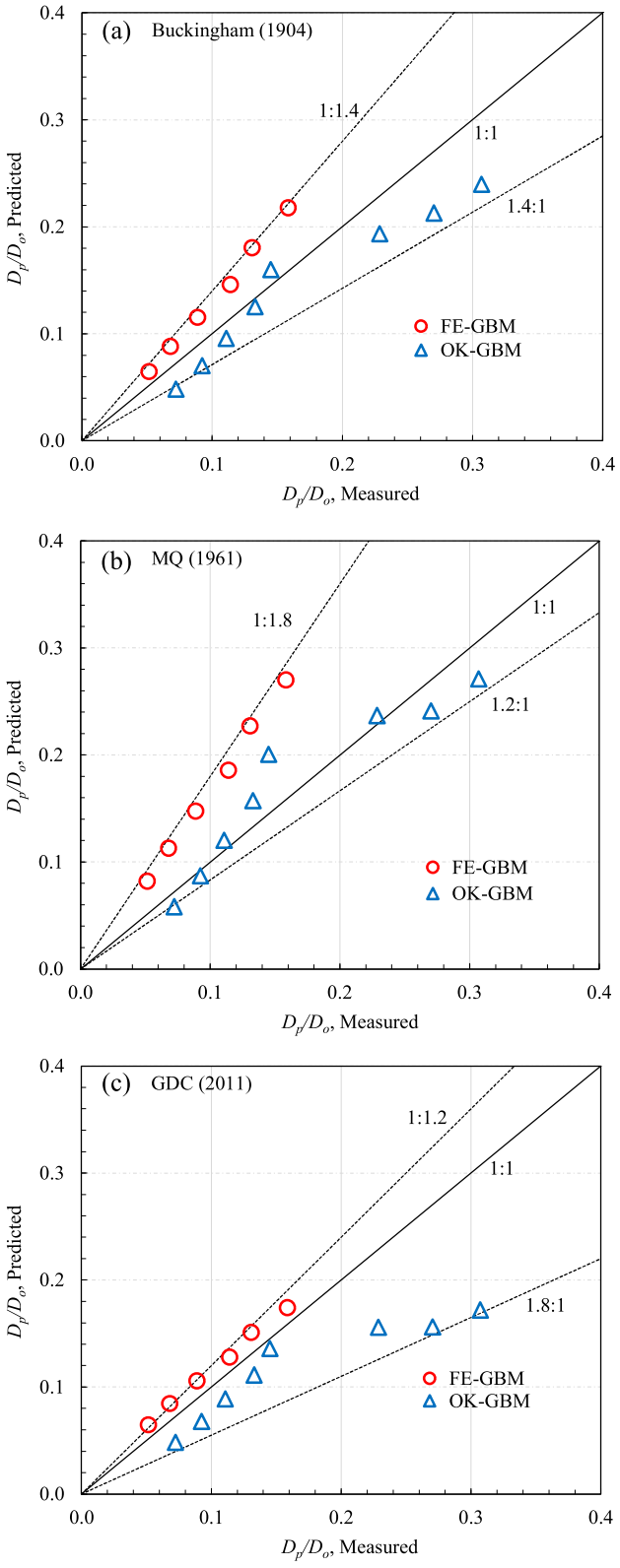

Fig. 8. Testing of three D_p/D_o models against the measured D_p/D_o data of FE-GBM and OK-GBM, (a) Buckingham (1904), (b) MQ (1961), and (c) GDC (2011).

$X_g = 2$). The observed maximum and average X_g values for the FE-GBM were 2.6 and 2.3, respectively. The X_g values of the OK-GBM samples lay between those of Marshall (1959, $X_g = 1.5$) and Buckingham (1904, $X_g = 2$) with an average X_g of 1.8. In comparison to other geomaterials, the GBM showed higher X_g values than sand or loams in the medium to fully compacted range, particularly the FE-GBM.

Table 3
Test of predictive D_p/D_o as function of ε against measured data. Calculated RMSE and bias are given.

Model	Equation	FE-GBM		OK-GBM	
		RMSE	Bias	RMSE	Bias
Buckingham (1904)	$D_p/D_o = \varepsilon^2$	0.037	0.033	0.036	−0.027
MQ (1961)	$D_p/D_o = \varepsilon^{10/3}/\Phi^2$	0.074	0.069	0.028	0.002
GDC (2011)	$D_p/D_o = 0.5\Phi(\varepsilon/\Phi)^3$	0.016	0.016	0.070	−0.053

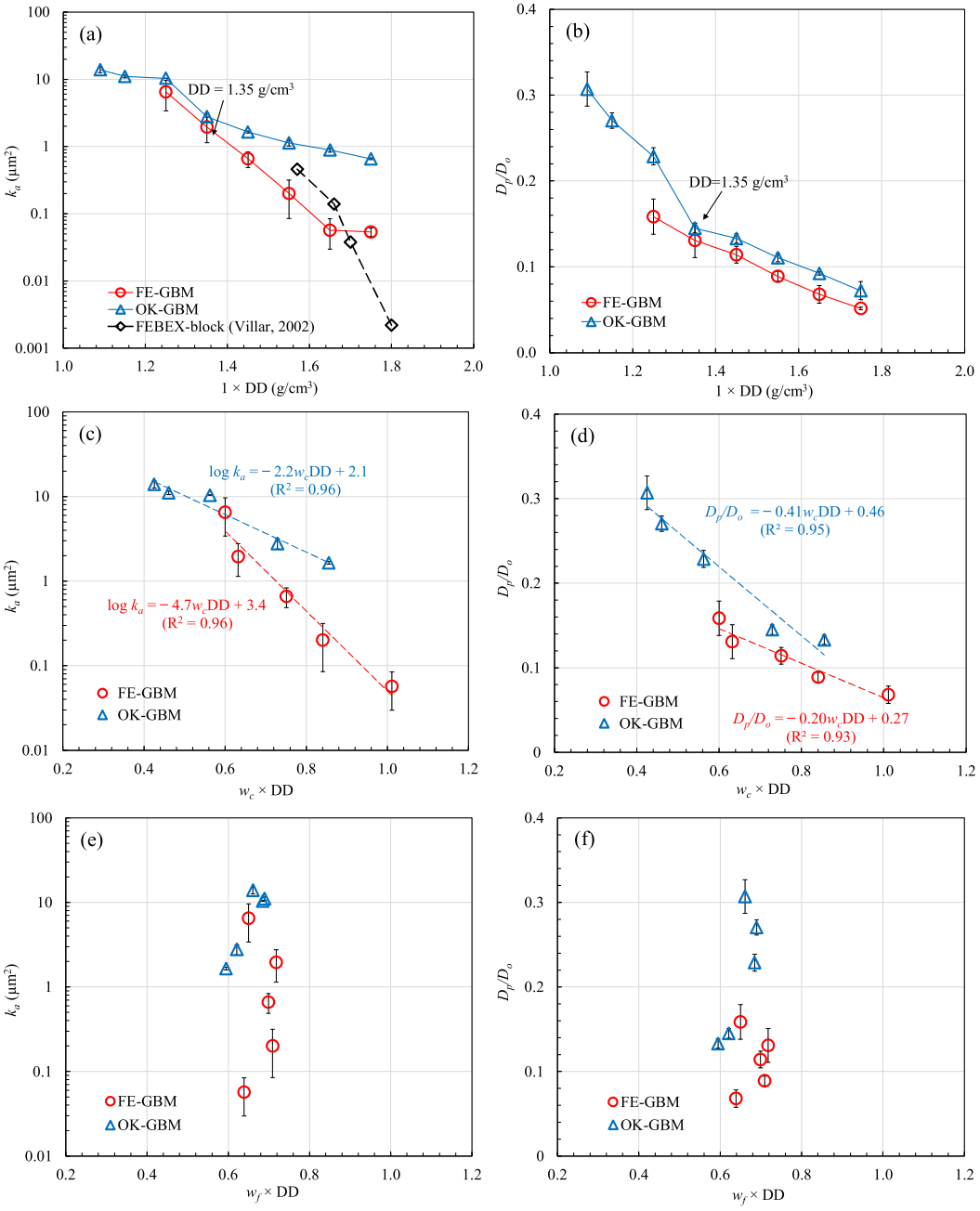

Fig. 9. Measured k_a and D_p/D_o as a function of (a, b) 1 × DD, (c, d) w_c × DD, and (e, f) w_f × DD.

At high ε (>0.4), the k_a values of the FE-GBM and the OK-GBM were almost equal (Fig. 6a). However, with a decreasing ε, the k_a of the FE-GBM drastically decreased. In the densely compacted range (low ε), the k_a of the OK-GBM was about 10-fold higher than that of the FE-GBM. One possible explanation could be that the larger d_{eq} and the least tortuous paths (or lower T) caused an enhanced advective flow (k_a) in the OK-GBM as compared to the FE-GBM under medium-dense to densely packed conditions (Lamb and Whitman, 1969; Moldrup et al., 2001). The reported k_a values of the compacted FEBEX bentonite samples (prepared by compressing the granular bentonite material sieved by the 5-mm mesh) are also plotted in Fig. 6a. The k_a values of the low dry density (DD < 1.7 g/cm^3, average moisture content of 7.3 %, and ε ranging from 0.23 to 0.30 cm^3/ cm^3) FEBEX-block sample are seen to be similar to the measured k_a values under the densely packed condition in the GBMs. The k_a values of the highly compacted (DD = 1.80 g/cm^3, moisture content of 12.4 %, and corresponding ε = 0.11 cm^3/cm^3) FEBEX block sample are very low, about 20-fold lower than the measured k_a values for the densely packed FE-GBM samples. The results showed that the diffusive transport through the GBM was controlled by the combined effect of T, X_g, and d_{eq}; however, T appeared to be dominant. At the low DD (higher ε) and similar pore sizes, the FE-GBM (although with higher X_g than OK-GBM) resulted in lower D_p/D_o due to the higher T. The effect of T was more dominant in the results of the OK-GBM, in which X_g was almost independent of ε, and the reduction in d_{eq} was not sharp, the D_p/D_o values of the OK-GBM drastically decreased from 0.3 to 0.07.

4.2.2. Adaptability of predictive $k_a(\varepsilon)$ and $D_p/D_o(\varepsilon)$ models

Fig. 6a shows the power law model fitted to the results of k_a for the materials used in this study. The power law model for k_a matched the observed k_a data well for the FE-GBM (R^2 = 0.97) and OK-GBM (R^2 = 0.93). However, the materials captured different model parameters: the α value of the FE-GBM (=2300) was about 10-fold higher than that of the OK-GBM (=200); similarly, the X_a of the FE-GBM (=8.3) was twice that of the OK-GBM (=4.1). The FE-GBM α value was close to the α (=2500) value observed by Wickramarachchi et al. (2011) for gravelly soil. The power law function was applied to the data of compacted FEBEX bentonite blocks (Villar, 2002); the α (=87) was about half that of the OK-GBM and the X_a (=4.9) was slightly higher than that of the OK-GBM.

The estimated D_p/D_o from the predictive models (Buckingham, MQ, and GDC) are plotted in Fig. 6b. Fig. 8 presents a scatterplot comparison of the measured and predicted D_p/D_o values along with the upper and lower predictive limits of these three models. The MQ (1961) provided the upper limit of the GBM data and predicted the OK-GBM data well. The GDC (2011) model provided the lower limit of the data and described the data for the FE-GBM well. The Buckingham model (1904) performed as a median of the data and tended to capture the OK-GBM samples packed at medium dense compaction (ε = 0.35 to 0.40). The D_p/D_o values predicted with the three models correlated well with the measured data and ranged within a factor of 1.8. The calculated RMSE and bias values of these models are presented in Table 3.

4.2.3. Linkage of MFXCT analysis with gas transport parameters

In order to develop a possible linkage between the MFXCT results and the gas transport parameters, k_a and D_p/D_o, representative indicators, a product of corresponding CT brightness weighting factors and sample DD, were introduced for both fractions, i.e., $w_f \times$ DD and $w_c \times$ DD, representing indicators for the fine and coarse fractions,

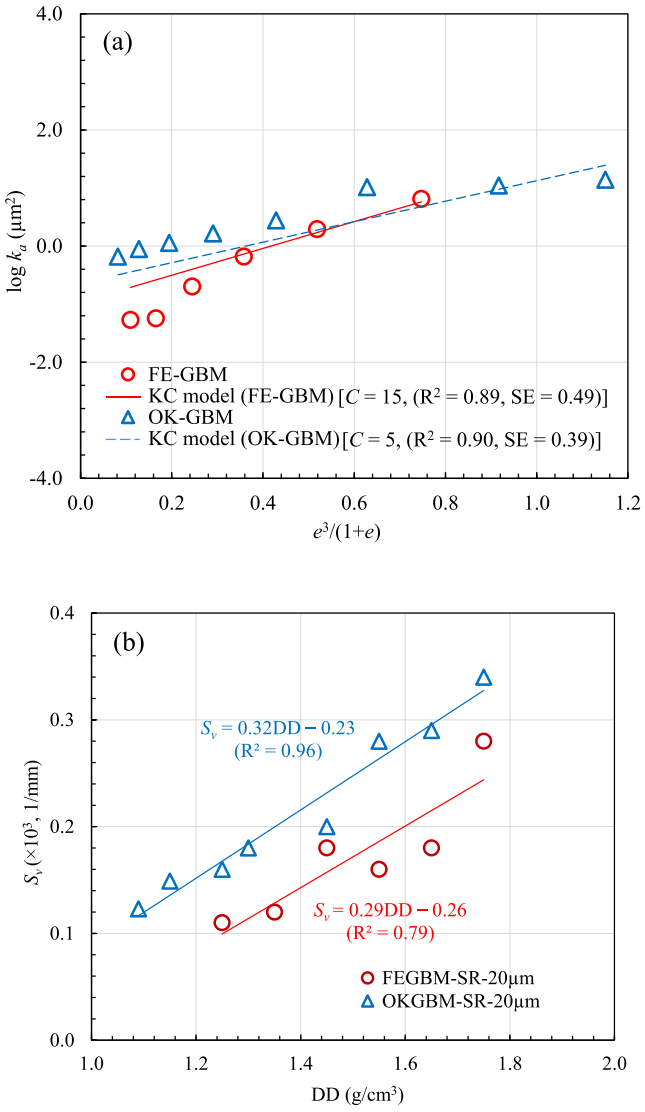

Fig. 10. (a) Correlation between measured log k_a as a function of $e^3/(1 + e)$ for FE-GBM and OK-GBM. (b) Measured S_v values as a function of DD. Predictive KC model by using measured S_v from MFXCT analysis are given in (a).

respectively. Fig. 9 shows the results of k_a and D_p/D_o plotted as functions of samples DD (1 × DD), w_c × DD, and w_f × DD. With increasing 1 × DD and w_c × DD, both k_a and D_p/D_o decreased at a similar rate (trend), as is noticeably evident from the solid (Fig. 9a and 9b) and dotted (Fig. 9c and 9d) lines. This observation suggests that the coarse size fractions acted as a controlling parameter for the gas transport through the GBM. The plot shows that a strong linear correlation exists between the coarse fraction indicator(w_c × DD) and k_a, and D_p/D_o, the equations are presented in Fig. 9c and 9d. The w_f × DD indicator was not well-correlated with the measured k_a and D_p/D_o (Fig. 9e and 9f). The detailed mechanism for the strong relationship between the gas transport parameters (k_a and D_p/D_o) and the MFXCT coarse fraction indicator (w_c × DD) has not been identified. Due to the limitations of the MFXCT measurement system, it was not possible to either distinguish the boundary between the coarse pellets and the fine fractions or to separate the fine fraction from the pore spaces. A more advanced technique or improvements in the MFXCT system may lead to the ability to distinguish specific sizes or the separation of the pores from the fines and to possibly explain the mechanisms.

4.2.4. Prediction of k_a using S_v measured by MFXCT

The KC model was tested against the measured k_a values for the FE-GBM and OK-GBM to confirm its applicability to granular mixtures under air-dried conditions. According to the KC equation, the k_a depends on C, S_v, and e, for which the adopted C values were based on best fitting, S_v was obtained by the MFXCT, and e was calculated from the basic phase relation equation. The measured S_v values of the FE-GBM and OK-GBM from the MFXCT are presented in Fig. 10b. The S_v increased linearly with the increasing DD in both mixtures, with a stronger linear correlation for the OK-GBM than the FE-GBM.

The measured and predicted (KC model) k_a values are shown as log k_a versus $e^3/(1+e)$ in Fig. 10a. The measured data plotted as an approximately straight line on the log k_a versus $e^3/(1+e)$ plot; k_a increased linearly with the increasing $e^3/(1+e)$. These results concur with the findings of many researchers (Lamb and Whitman, 1969) and the experimental results for FEBEX bentonite (Villar, 2004). The KC model predicted the measured k_a of the mixtures well, at the fitted C values of 5 (for the OK-GBM) and 15 (for the FE-GBM), as is evident from the predictive lines, with higher R^2 and low standard error (SE) values. The adopted C (=5) value for the OK-GBM in this work conforms to that of many researchers, including Carman (1937). The higher fitted C value (=15) in the FE-GBM indicates that the flow through the FE-GBM is greatly controlled by the pore and tortuosity indices. This observation substantiates the findings discussed in the previous section. The above results indicate that the KC model can be used to predict the permeability characteristics of GBMs.

5. Conclusions

The effect of dry density on the gas transport (convective and diffusive) characteristics of air-dried granulated bentonite mixtures (GBMs), prepared with bentonites originating from the USA (FE-GBM) and Japan (OK-GBM), were investigated. From a material characterization perspective, the swelling ability of the FE-GBM was higher than that of the OK-GBM due to its high montmorillonite content. The air permeability (k_a) and gas diffusivity (D_p/D_o) were found to decrease with an increasing dry density (DD). The OK-GBM showed higher k_a and D_p/D_o values than the FE-GBM due to larger pore diameters and lower tortuosity. The gas transport through the GBMs was highly controlled by the identified pore structural parameters, including the pore diameter, tortuosity, and pore connectivity-tortuosity. The power law model matched the measured k_a data well. The existing predictive D_p/D_o models were able to capture the measured D_p/D_o data within a factor of 1.8. The Kozeny-Carman (KC) model was found to be applicable for the prediction of the k_a characteristics of GBMs.

MFXCT results provided visual and quantitative information (based on the CT brightness) to aid in the understanding of the compaction characteristics of GBMs. From the linkage, a good linear correlation was obtained between the MFXCT coarse fraction indicator and the gas transport parameters, k_a and D_p/D_o. One limitation of the method is that the boundary between the coarse pellets and the fine size fractions could not be defined. This suggests the need for the development of more sophisticated and advanced techniques or improvements in MFXCT systems in order to help with the separation of the pellets and fractions into specific sizes.

Declaration of Competing Interest

The authors declare that they have no known competing financial interests or personal relationships that could have appeared to influence the work reported in this paper.

Acknowledgments

This work was partially supported by a JST-JICA Science and Technology Research Partnership for Sustainable Development (SATREPS) project and was made possible by the 'Providing New Insight into Interactions Between Soil Functions and Structure' (PROTINUS)-project in the framework of H2020. The authors are thankful to NAGRA, Switzerland for providing the FE-GBM to carry out this research work.

Appendix A. (Fig. A1, Fig. A2).

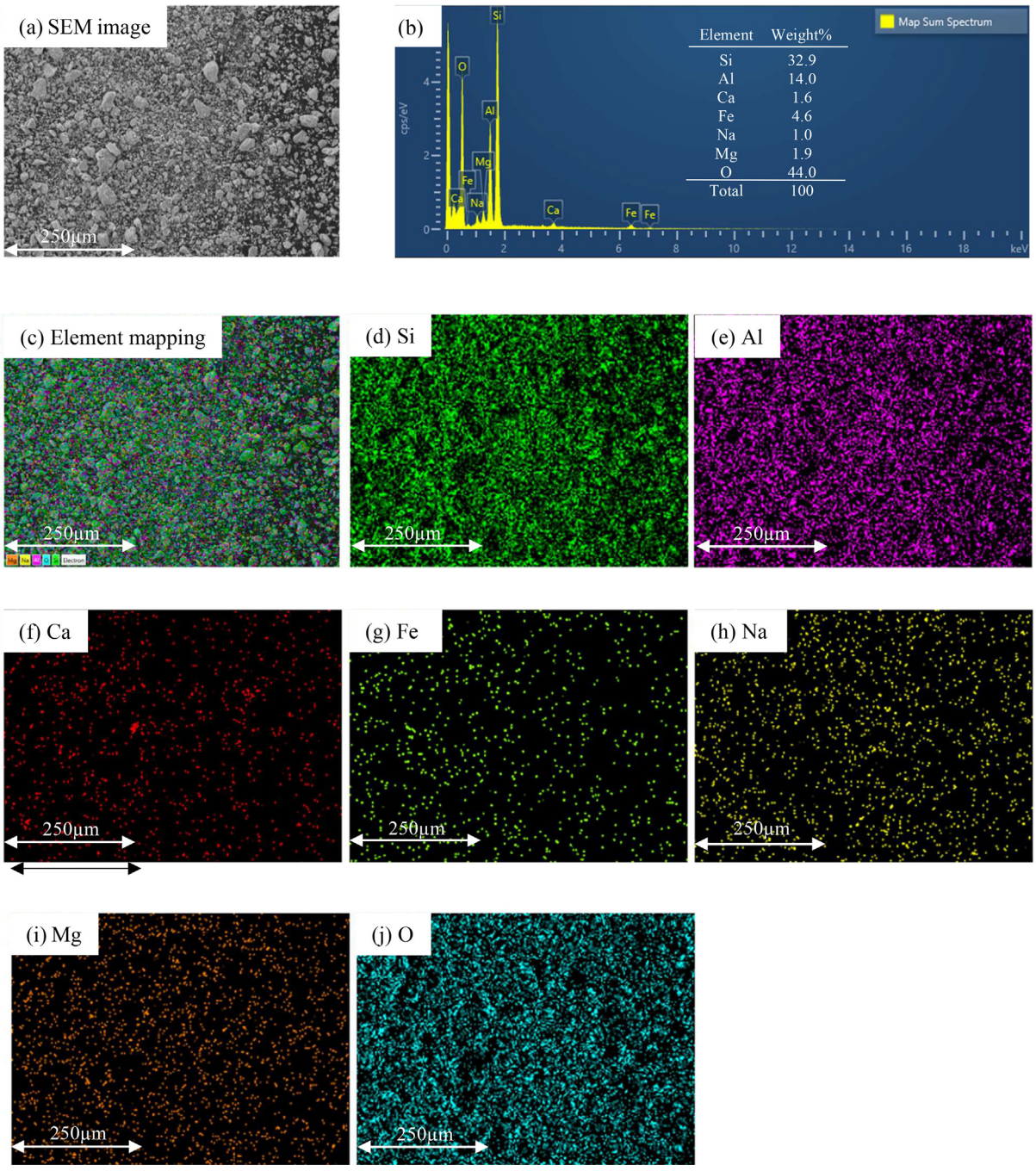

Fig. A1. FE-GBM: SEM image and element mapping and spectrum by EDS analyzer (Grain size of < 0.106 mm;Magnification of scanning is × 200).

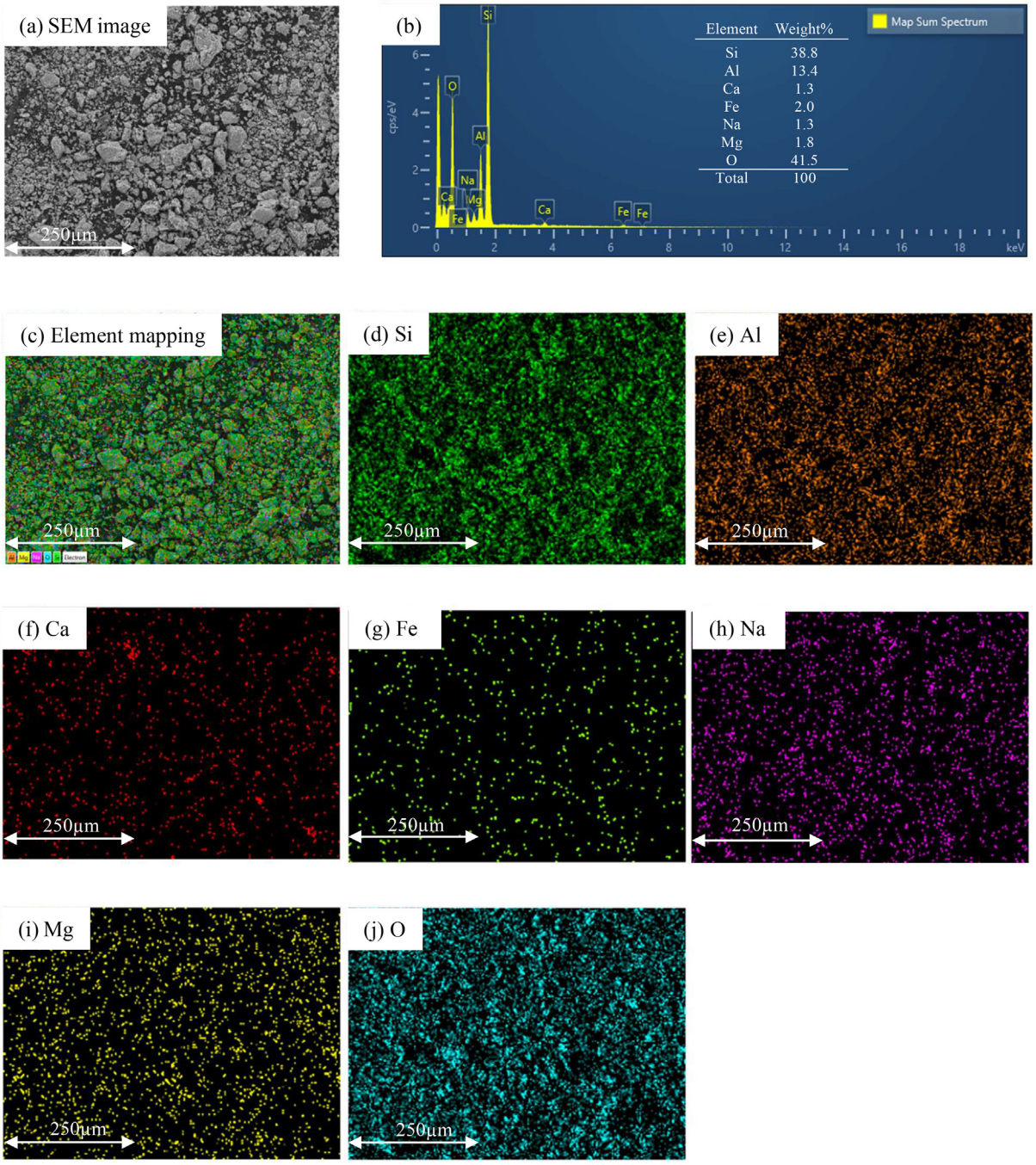

Fig. A2. OK-GBM: SEM image and element mapping and spectrum by EDS analyzer (Grain size of < 0.106 mm;Magnification of scanning is × 200).

References

Alonso, E.E., Hoffmann, C., Romero, E., 2010. Pellet mixtures in isolation barriers. J. Rock Mech. Geotech. Eng. 2 (1), 12–31.

Arthur, R., Sasamoto, H., Yui, M., 2004. Potential complications in the development of a thermodynamic database for hyperalkaline, argillaceous systems, Proceedings of the Int. Workshop on Bentonite-Cement Interaction in Repository Env., Nuclear Waste Management Org. Jpn. (NUMO). NUMO-TR-04-05, October.

Ball, B.C., 1981. Modelling of soil pores as tubes using gas permeabilities, gas diffusivities and water release. J. Soil Sci. 32 (4), 465–481.

Barrett, E.P., Joyner, L.G., Halenda, P.H., 1951. The determination of pore volume and area distributions in porous substances. I. Computations from nitrogen isotherms. J. Am. Chem. Soc. 73, 373–380.

Brunauer, S., Emmet, P.S., Teller, E., 1938. Adsorption of gases in multimolecular layers. J. Am. Chem. Soc. 60, 309–319.

Buckingham, E., 1904. Contributions to our knowledge of the aeration of soils. USDA. Bur. Soil Bul. 25. U.S. Gov. Print. Off., Washington, DC.

Carbonell, B., Villar, M.V., Martín, P.L., Gutiérrez-Álvarez, C., 2019. Gas transport in compacted bentonite after 18 years under barrier conditions. Geomech. Energy Env. 17, 66–74.

Carman, P.C., 1937. Fluid flow through granular beds. Trans. Inst. Chem. Eng. 15, 150.
Carman, P.C., 1938. The determination of the specific surface of powders. J. Soc. Chem. Ind. Trans. 57, 225.
Carman, P.C., 1956. Flow of gases through porous media. Butterworths Scient. Pub, London.
Chamindu Deepagoda, T.K.K., Moldrup, P., Schjønning, P., Kawamoto, K., Komatsu, T., de Jonge, L.W., 2011. Generalized density-corrected model for gas diffusivity in variably saturated soils. Soil Sci. Soc. Am. J. 75 (4), 1315–1329.
Coulon, H., 1987. Propriétés physico-chimiques de sédiments argileux français: contribution au stockage de déchets radioactifs. Ph.D. Thesis. Université Des Sciences Et Techniques De Lille Flandres-Artois (in French).
Cui, Y.J., Tang, A.M., Qian, L.X., Ye, W.M., Chen, B., 2011. Thermal-mechanical behavior of compacted GMZ bentonite. Soils Found. 51 (6), 1065–1074.
Currie, J.A., 1960. Gaseous diffusion in porous media: Part 1. A non-steady state method. Br. J. App Phys. 11, 314–317.
De Bock, C., Bosgiraud, J.M., Breen, B., Johnson, M., Rothfucs, T., Weber, H., Van Marcke, P., Verstricht, J., 2009. Module 1 (Buffer construction technology). Final report. ESDRED Project Deliverable Mod1-WP6-D6. EU report.
Dixon, D., Sandén T., Jonsson E., Hansen J., 2011. Backfilling of deposition tunnels: Use of bentonite pellets. SKB. Feb. P-11-44, ISSN 1651-4416.
ENRESA, 2000. Full-scale engineered barriers experiment for a deep geological repository for high-level waste in crystalline host rock. Final report, Tech. Pub. ENRESA 01/2000, Madrid, 354.
Fuller, W.B., Thompson, S.E., 1907. The laws of proportioning concrete. Transactions of the Am. Soc, Civil Engineers LIX, Paper, p. 1053.
García-Siñeriz, J.L., Villar, M.V., Rey, M., Palacios, B., 2015. Engineered barrier of bentonite pellets and compacted blocks: State after reaching saturation. Eng. Geol. 192, 33–45.
Garitte, B., Weber, H., Müller, H.R., 2015. Requirements, manufacturing and QC of the buffer components. Report LUCOEX - WP2. Deliverable (D2.3), 473 pp
Giroud, N., Tomonaga, Y., Wersin, P., Briggs, S., King, F., Vogt, T., Diomidis, N., 2018. On the fate of oxygen in a spent fuel emplacement drift in Opalinus clay. Appl. Geochem. 97, 270–278.
Glinski, J., Stepniewski, W., 1985. Soil aeration and its role for plants. CRC Press, Boca Raton, FL.
Guillot, X., Al-Mukhtar, M., Bergaya, F., Fleureau, J.M., 2002. Estimation de la porositáe dans un matáeriau argileux, C.R. Geosci. 334, 105–109.
Hamamoto, S., Moldrup, P., Kawamoto, K., Komatsu, T., 2009. Effect of particle size and soil compaction on gas transport parameters in variably saturated, sandy soils. Vadose. Zone J. 8 (4), 986–995.
Hamamoto, S., Moldrup, P., Kawamoto, K., Sakaki, T., Nishimura, T., Komatsu, T., 2016. Pore network structure linked by X-ray CT to particle characteristics and transport parameters. Soils Found. 56 (4), 676–690.
Harrington, J.F., Graham, C.C., Cuss, R.J., Norris, S., 2019. Gas network development in compact bentonite: key controls on the stability of flow pathways. Geofluids.
Hoffmann, C., Alonso, E.E., Romero, E., 2007. Hydro-mechanical behaviour of bentonite pellet mixtures. Phy. Chem. Earth 32, 832–849.
Imbert, C., Villar, M.V., 2006. Hydro-mechanical response of a bentonite pellets/powder mixture upon infiltration. App. Clay Sci. 32, 197–209.
Japan Nuclear Cycle Development Institute, 2000. H12: Project to establish the scientific and technical basis for HLW disposal in Japan, Supporting Report 2, Repository Design and Eng. Tech. Second Progress Report on Res. Development for the Geol. Disposal of HLW in Japan. JNC TN1410 2000-003.
Iversen, B.V., Schjønning, P., Poulsen, T.G., Moldrup, P., 2001. In situ, on-site and laboratory measurements of soil air permeability: boundary conditions and measurement scale. Soil Sci. 166 (2), 97–106.
Karnland, O., Nilsson, U., Weber, H., Wersin, P., 2008. Sealing ability of Wyoming bentonite pellets foreseen as buffer material - laboratory results. Phys. Chem. Earth 33, 472–475.
Kawamoto, K., Moldrup, P., Schjønning, P., Iversen, B.V., Komatsu, T., Rolston, D.E., 2006. Gas transport parameters in the vadose zone: development and tests of power-law models for air permeability. Vadose Zone J. 5 (4), 1205–1215.
Komine, H., 2004. Simplified evaluation for swelling characteristics of bentonites. Eng. Geol. 71, 265–279.
Kozeny, J., 1927. Ueber kapillare leitung des wassers im boden. Sitzungsber. Akad Wiss Wien 136, 271–306.
Lambe, T.W., Whitman, R.V., 1969. Soil Mechanics. John Wiley & Sons, New York.
Liu, Z.R., Cui, Y.J., Ye, W.M., Chen, B., Wang, Q., Chen, Y.G., 2020. Investigation of the hydro-mechanical behaviour of GMZ bentonite pellet mixtures. Acta Geotech. 15 (10), 2865–2875.
Liu, J.F., Skoczylas, F., 2014. Experimental research on water retention and gas permeability of compacted bentonite/sand mixtures. Soils Found. 54 (5), 1027–1038.
Liu, J.F., Song, Y., Skoczylas, F., Liu, J., 2015. Gas migration through water-saturated bentonite–sand mixtures, COx argillite, and their interfaces. Can. Geotech. J. 52, 1–12.
Liu, J.F., Skoczylas, F., Talandier, J., Pu, H., 2016. Dismantling of the EB experiment: experimental research on the retrieved GBM and bentonite blocks. Nucl. Eng. Des. 300, 297–307.
Marshall, T.J., 1959. The diffusion of gases through porous media. J. Soil Sci. 10, 79–82.
Masuda, R., Asano, H., Toguri, S., Mori, T., Shimura, T., Matsuda, T., Uyama, M., Noda, M., 2007. Buffer construction technique using granular bentonite. J. Nuclear Sci. Tech. 44 (3), 448–455.
Mayor, J., García-Siñeriz, J., Alonso, E., Alheid, H., Blümling, P., 2005. Engineered barrier emplacement experiment in Opalinus Clay for the disposal of radioactive waste in underground repositories. Empresa Nacional de Residuos Radiactivos. Jan, ENRESA, pp. 1–101.
Millington, R.J., Quirk, J.M., 1960. Transport in porous media. p. 97–106. In F.A. Van Beren et al (ed.) Trans. Int. Congr. Soil Sci., 7th, Madison, WI. 14–21 Aug. 1960. Vol. 1. Elsevier, Amsterdam.
Millington, R. J., Quirk, J.M., 1961. Permeability of porous solids. Trans. Faraday Soc. 57, 1200–1207.
Moldrup, P., Olesen, T., Komatsu, T., Schjønning, P., Rolston, D.E., 2001. Tortuosity, diffusivity, and permeability in the soil liquid and gaseous phases. Soil Sci. Soc. Am. J. 65 (3), 613–623.
Moldrup, P., Yoshikawa, S., Olesen, T., Komatsu, T., Rolston, D.E., 2003. Air permeability in undisturbed volcanic ash soils. Soil Sci. Soc. Am. J. 67 (1), 32–40.
Müller, H.R., Garitte, B., Vogt, T., Köhler, S., Sakaki, T., Weber, H., Spillmann, T., Hertrich, M., Becker, J., Giroud, N., Cloet, V., Diomidis, N., Vietor, T., 2017. Implementation of the full-scale emplacement (FE) experiment at the Mont Terri rock laboratory. Swiss J. Geosc. 110 (1), 287–306.
NAGRA, 2019. Implementation of the full-scale emplacement experiment at Mont Terri: Design, construction and preliminary results. Technical report 15-02. May. Nagra, Wettingen (Switzerland).
Nakashima, H., Saito, A., Ishii, T., 2014. Method for producing high-density bentonite pellets using dry shrinkage. J. Nucl. Fuel Cycle Env. 21 (2), 83–94, in Japanese.
Nazir, M., Kawamoto, K., Sakaki, T., 2021a. Properties of granulated bentonite mixtures for radioactive waste disposal: a review. Int. J. GEOMATE 20 (81), 132–145.
Nazir, M., Matsuno, A., Saito, T., Kawamoto, K., Sakaki, T., 2021b. Visualization of microstructure and measurement of mass transport parameters for granulated bentonite mixtures. Jpn. Geotech. Soc. Special Publication 9 (2), 26–30.
Osozawa, S., 1987. Measurement of soil-gas diffusion coefficient for soil diagnosis. Soil Phys. Cond. Plant Growth 55, 53–60.
Otani, J., Mukunoki, T., Obara, Y., 2000. Application of X-ray CT method for characterization of failure in soils. Soils Found. 40 (2), 111–118.

Plötze, M., Weber, H.P., 2007. ESDRED: Emplacement tests with granular bentonite MX-80: laboratory results from ETH Zürich. Nagra. Working Rep. NAB, 7–24.

Rolston, D. E., Moldrup, P., 2002. Chapter 4.3. Gas Diffusivity. In: Dane, J.H., Topp, G.C., (eds.), Methods of Soil Analysis, Part 4, SSSA Book Ser. 5. ASA and SSSA. Madison, WI, pp. 1113–1139.

Sakaki, T., Firat Lüthi, B., Vogt, T., Uyama, M., Niunoya, S., 2019. Heated fiber-optic cables for distributed dry density measurements of granulated bentonite mixtures: feasibility experiments. Geomech. Energy Env. 17, 57–65.

Sakaki, T., Firat Lüthi, B., Vogt, T., 2022. Investigation of the emplacement dry density of granulated bentonite mixtures using dielectric, mass-balance and actively heated fiber-optic distributed temperature sensing methods. Geomech. Energy Environ. 100329. https://doi.org/10.1016/j.gete.2022.100329.

Sugita, Y., Suzuki, H., Chijimatsu, M., 2003. Thermal, hydraulic and swelling properties of bentonite pellet – Examine on calculating parameter assessment on PRP. Research Document. JNC, TN8400 2002–023.

Suzuki, H., Shibata, M., Yamagata, J., Hirose, I., Terakado, K., 1992. Characteristics of test of buffer material (I). Power Reactor and Nuclear Fuel Development Corporation. PNC TN8410 92-057 (in Japanese)

Tang, A.M., Cui, Y.J., 2005. Controlling suction by the vapour equilibrium technique at different temperatures and its application in determining the water retention properties of MX80 clay. Can. Geotech. J. 42 (1), 287–296.

Villar, M.V., Lloret, A., 2008. Influence of dry density and water content on the swelling of a compacted bentonite. App. Clay Sci. 39, 38–49.

Villar, M.V., Gutiérrez-Rodrigo, V., Martín, P.L., Romero, F.J., Barcala, J.M., 2013. Gas transport in bentonite. Technical Report, Informes Técnicos Ciemat, December, p. 65.

Villar, M.V., Lloret, A., 2001. Variation of the intrinsic permeability of expansive clays upon saturation. In: Adachi, K., Fukue, M. (Eds.), Clay Science for Engineering. Balkema, Rotterdam, pp. 259–266.

Villar, M.V., Martín, P.L., Romero, F.J., Iglesias, R.J., Gutiérrez-Rodrigo, V., 2016. Saturation of barrier materials under thermal gradient. Geomech. Energy Env. 8, 38–51.

Villar, M.V., 2002. Thermo-hydro-mechanical characterisation of a bentonite from Cabo de Gata. A study applied to the use of bentonite as sealing material in high level radioactive waste repositories. Publicación Técnica ENRESA 01/2002. pp. 258. Madrid.

Villar, M.V., 2004. Thermo-hydro-mechanical characteristics and Processes in the clay barrier of a high-level radioactive waste repository. Report. Informes Técnicos Ciemat. 1044, October, 75 pp.

Villar, M.V., 2013. Long-term performance of engineered barrier systems (PEBS); Long-term THM tests reports: Isothermal infiltration tests with materials from the HEE, CIEMAT Technical Report, CIEMAT/DMA/2G210/07/2013, December.

Volckaert, G., Dereeper, B., Put, M., Ortiz, L., Gens, A., Vaunat, J., Villar, M.V., Martin, P.L., Imbert, C., Lassabatere, T., Mouche, E., Cany, F., 2000. A large-scale in situ demonstration test for repository sealing in an argillaceous host rock. Reseal Project-Phase I. EUR 19612. Nuclear Sci. Tech. Series, Europ. Communities, Luxembourg. pp. 273

Wersin, P., Johnson, L.H., McKinley, I.G., 2007. Performance of the bentonite barrier at temperatures beyond 100 °C: a critical review. Phy. Chem. Earth 32, 780–788.

Wickramarachchi, P., Kawamoto, K., Hamamoto, S., Nagamori, M., Moldrup, P., Komatsu, T., 2011. Effects of dry bulk density and particle size fraction on gas transport parameters in variably saturated landfill cover soil. Waste Manage. 31 (12), 2464–2472.

Wieczorek K., Czaikowski O., Miehe, R., 2014. Long-term performance of engineered barrier systems (PEBS). GRS Participation. Report. GRS–353, December.

Yamada, A., Akiyama, Y., Nakajima, M., Yada, T., Chijimatsu, M., Nakajima, T., 2014. Studies of construction methods for bentonite engineered barrier systems for sub-surface disposal: vibratory compaction. Geol. Soc. Sp. Pub. 400 (1), 135–144.

Yong, R.N., Boonsinsuk, P., Wong, G., 1986. Formulation of backfill material for a nuclear fuel waste disposal vault. Can. Geotech. J. 23 (2), 216–228.